Nano-Micro Lett. (2018) 10:71
https://doi.org/10.1007/s40820-018-0225-1

ARTICLE

Nitrogen-Doped TiO_2–C Composite Nanofibers with High-Capacity and Long-Cycle Life as Anode Materials for Sodium-Ion Batteries

Su Nie[1] · Li Liu[1,2] · Junfang Liu[1] · Jianjun Xie[1] · Yue Zhang[1] · Jing Xia[1] · Hanxiao Yan[1] · Yiting Yuan[1] · Xianyou Wang[1]

Received: 19 July 2018 / Accepted: 20 September 2018 / Published online: 9 October 2018

Highlights

- Nitrogen-doped TiO_2–C composite nanofibers (TiO_2/N–C NFs) are fabricated using green, inexpensive urea as a nitrogen source and pore-forming agent.
- X-ray photoelectron spectroscopy results reveal changes in the content of different nitrogen species in detail.
- The TiO_2/N–C NFs anode exhibits excellent sodium storage performance.

Abstract Nitrogen-doped TiO_2–C composite nanofibers (TiO_2/N–C NFs) were manufactured by a convenient and green electrospinning technique in which urea acted as both the nitrogen source and a pore-forming agent. The TiO_2/N–C NFs exhibit a large specific surface area (213.04 $m^2\ g^{-1}$) and a suitable nitrogen content (5.37 wt%). The large specific surface area can increase the contribution of the extrinsic pseudocapacitance, which greatly enhances the rate capability. Further, the diffusion coefficient of sodium ions (D_{Na+}) could be greatly improved by the incorporation of nitrogen atoms. Thus, the TiO_2/N–C NFs display excellent electrochemical properties in Na-ion batteries. A TiO_2/N–C NF anode delivers a high reversible discharge capacity of 265.8 mAh g^{-1} at 0.05 A g^{-1} and an outstanding long cycling performance even at a high current density (118.1 mAh g^{-1}) with almost no capacity decay at 5 A g^{-1} over 2000 cycles. Therefore, this work sheds light on the application of TiO_2-based materials in sodium-ion batteries.

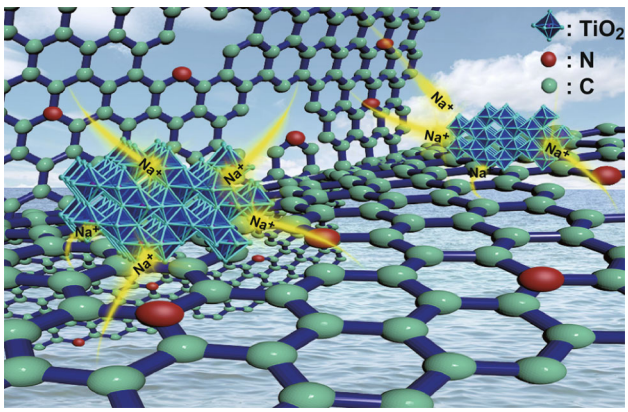

Keywords Nanofibers · Anode materials · Sodium-ion batteries · Pseudocapacitance · Nitrogen-doping

Electronic supplementary material The online version of this article (https://doi.org/10.1007/s40820-018-0225-1) contains supplementary material, which is available to authorized users.

✉ Li Liu
liulili1203@126.com

[1] National Base for International Science and Technology Cooperation, National Local Joint Engineering Laboratory for Key Materials of New Energy Storage Battery, Hunan Province Key Laboratory of Electrochemical Energy Storage and Conversion, School of Chemistry, Xiangtan University, Xiangtan 411105, People's Republic of China

[2] Key Laboratory of Advanced Energy Materials Chemistry (Ministry of Education), Nankai University, Tianjin 300071, People's Republic of China

1 Introduction

In recent decades, lithium-ion batteries (LIBs) play an important role in daily life (for example, in electric/hybrid vehicles and portable electronic products) owing to their excellent energy densities and long life spans [1–5]. Nevertheless, the disadvantages of limited lithium resources and high costs limit the commercial application of LIBs in large-scale energy storage. In contrast, sodium-ion batteries (SIBs) are more suitable for low-cost energy storage devices because of the abundance of sodium and affordable price [6–9]. Nevertheless, it is still challenging to find a suitable host material with a larger space suitable for sodium ion insertion/extraction, which is necessary because the Na^+ ion (1.06 Å) is ca. 40% larger than the Li^+ ion (0.76 Å) [10, 11]. Therefore, it is vital to investigate suitable electrode materials for SIBs.

There are many reports on anode materials for SIBs, including alloying/dealloying reaction materials (Sn, Sb) [12, 13], conversion reaction materials (FeS_2, Fe_2O_3) [14, 15], and insertion/extraction reaction materials ($Na_2Ti_3O_7$, TiO_2) [16, 17]. In particular, anatase titanium dioxide (TiO_2), with a high natural abundance, nontoxicity, a small volume change (less than 4%), and low production cost, has attracted extensive attention as a promising anode material for SIBs [18]. However, TiO_2 has inherent defects, such as inferior electrical conductivity (10^{-12} S cm^{-1}) as well as narrow ionic channels that cannot support rapid transfer of sodium ions [19–21], resulting in low specific capacity and serious capacity loss at high current densities. In order to improve its sodium storage performance, an important strategy is to increase its conductivity. One typical approach is to decrease the size of TiO_2 particles or design novel nanostructures such as nanowires [22], nanospheres [23], or nanotubes [24], which can greatly shorten the sodium ion diffusion distance and promote electronic transport. Another effective method is recombination with carbon or doping of multivalent ions with Fe [25], S [26], Nb [27], or N [28].

Recently, nitrogen doping has been reported as an effective method to increase both the electronic and ionic conductivities of bulk materials [29, 30]. Nitrogen-doped carbon hollow spheres and carbon nanofibers (NFs) have exhibited excellent electrochemical properties as anode materials for SIBs [31, 32]. Nitrogen doping is effective not only for carbon materials, but also for transition-metal-oxide-based carbon composites. Some nitrogen-doped carbon composite transition metal oxides (such as MnO [33], Fe_2O_3 [34], Co_3O_4 [35], and TiO_2 [36]) have been reported and showed satisfactory results. However, at present, the common methods of introducing N atoms are to calcine bulk materials in a poisonous atmosphere of N_2/NH_3 or to use rare and expensive nitrogen-rich materials, such as 3-hydroxytyramine hydrochloride, diethylenetriamine, polyaniline, and polypyrrole as nitrogen sources.

As a convenient and universal technology for producing polymers or composite material NFs, the electrospinning method has been widely applied in both academic research and industrial applications. Very recently, there have been many studies on the preparation of high-performance electrode materials (such as SnS/C, Na_2VPO_4F/C, and NiO/C) by electrospinning technology [37–39]. The obtained one-dimensional NFs with high specific surface areas can provide facile electronic and ionic transport. Further, the porous structure is highly tolerant of stress changes during the reaction in the battery, making it conducive to the realization of a long cycle life [39, 40].

Herein, a simple, economical, and green electrospinning process is proposed to obtain nitrogen-doped TiO_2–C composite NFs (denoted as TiO_2/N–C NFs). Inexpensive urea is used as the nitrogen source and pore-forming agent. Owing to the advantages of nitrogen doping and the large specific surface area, a TiO_2/N–C NF electrode displays outstanding electrochemical properties.

2 Experimental Section

2.1 Synthesis of Materials

The TiO_2/N–C NFs were synthesized by electrospinning followed by high-temperature carbonization. The precursor solution for electrospinning was made as follows: First, 5.0 mL of *N*, *N*-dimethylformamide (Kermel, 99.5%) and 1.05 g of glacial acetic acid (CH_3COOH, Kermel, 99.5%) were mixed; then, 0.1 g of urea [$CO(NH_2)_2$, Kermel, 99.5%] and 0.97 g of tetra-n-butyl titanate ($C_{16}H_{36}O_4Ti$, Kermel, 99%) were added with stirring. Next, 0.4 g of polyvinylpyrrolidone (PVP, Mw = 1,300,000, Alfa Aesar) was added to the above mixed solution under stirring for 12 h to acquire a clear precursor solution. The obtained solution was injected into a 10-mL syringe connected to a blunt-tip needle and spun on an electrospinning unit with an applied voltage of 14 kV. The distance between the needle and the collector was set to 14 cm, and the flow velocity was 0.36 mL h^{-1}. The collected NFs were dried at 70 °C for 8 h in a vacuum oven and then precalcined at 200 °C for 2 h. Finally, the TiO_2/N–C composite NFs were obtained by calcination at 550 °C for 4 h in an inert atmosphere of Ar, where the ramping rate was set to 4 °C min^{-1}.

For comparison, the pristine TiO_2–C NFs and the other two types of TiO_2/N–C NFs with different N contents were prepared using similar methods by adjusting the amount of urea to 0, 0.05, and 0.2 g, respectively.

2.2 Structural Characterization

The as-prepared materials were examined by X-ray diffraction (XRD) in a Rigaku D/Max-2500 powder diffractometer with Cu $K\alpha$ radiation (λ = 1.5418 Å). The morphologies of the synthesized samples were observed using scanning electron microscopy (SEM, JEOL, SM-71480) and transmission electron microscopy (TEM, JEOL, JEM-100CX). The chemical composition of the as-prepared materials was analyzed using X-ray photoelectron spectroscopy (XPS, ThermoFisher, K-Alpha$^+$). N_2 adsorption–desorption isotherms were obtained using TriStar II 3020 (Micromeritics, USA) at liquid nitrogen temperature (77.3 K). The specific surface area (S_{BET}) was calculated by the conventional Brunauer–Emmett–Teller (BET) method. Thermogravimetry was performed using a TGA Q50 (TA Instruments) analyzer. Raman spectra were obtained using a Raman spectrometer (Renishaw, Model 1000) at an excitation wavelength of 514 nm.

2.3 Electrochemical Measurements

Polyvinylidene fluoride binder (10 wt%), 20 wt% carbon black, and 70 wt% active material (TiO_2/N–C NFs or TiO_2–C NFs) were dissolved in an appropriate amount of *N*-methyl-2-pyrrolidinone. The obtained slurry was evenly coated on copper foil and placed in a vacuum oven at 110 °C for 12 h. Circular pieces 1 cm in diameter were punched from the dried copper foil and used as working electrodes; their mass load was 1.2 ± 0.2 mg cm^{-2}. In an argon-filled glove box, CR2025-type coin cells were assembled; metallic sodium was used as the counter electrode and separated from the work electrode by a glass fiber (Whatman, GF/C). The electrolyte was a solution of 1 mol L^{-1} $NaClO_4$ dissolved in propylene carbonate/ethylene carbonate (1:1 by volume). The coin cells were cycled in galvanostatic discharge–charge measurements using a battery testing system (Neware, China) at room temperature at voltage intervals of 0.01 and 2.5 V. Both cyclic voltammetry (CV) tests and electrochemical impedance spectroscopy (EIS) experiments were conducted on a CHI660E electrochemistry workstation (Chenhua, Shanghai).

3 Results and Discussion

Figure 1a shows the XRD patterns of the TiO_2/N–C NFs and TiO_2–C NFs. All the peaks of both the TiO_2/N–C NFs and TiO_2–C NFs are in good agreement with those of anatase TiO_2 (JCPDS No. 21-1272). No peaks from other phases were observed, demonstrating the high purity of the as-prepared samples. The weak intensity of the TiO_2 peaks may be attributed to TiO_2 nanoparticles embedded in an amorphous carbon matrix, which will be further demonstrated in the TEM results below [18]. The Raman spectra in Fig. 1b reveal two obvious peaks at 1350 and 1600 cm^{-1}, which correspond to a disorder-induced feature (the D band) and the E_{2g} mode of graphite (the G band), respectively. An intensity ratio of the D/G bands ($I_D/I_G < 1.0$) can be used to identify a certain degree of graphitization in a carbon matrix [41–44]. The I_D/I_G values of the TiO_2/N–C NFs and TiO_2–C NFs are 0.843 and 0.828, respectively, which indicate high-quality electrical conductivity. In addition, a slight increase in the value of I_D/I_G (which corresponds to increasing disorder) may be related to the introduction of nitrogen, which caused defects and disordered structure in the carbon layer.

N_2 adsorption–desorption measurements were taken to determine the BET surface area and pore distribution of the TiO_2/N–C NFs and TiO_2–C NFs. In Fig. 1c, d, the BET surface area and average pore width of the TiO_2/N–C NFs are 213.04 m^2 g^{-1} and 3.4 nm, whereas the TiO_2–C NFs show a BET surface area and average pore width of 161.3 m^2 g^{-1} and 2.5 nm, respectively. The increased specific surface area and average pore width may be due to decomposition of urea during the heating process, as shown in Eq. 1:

$$CO(NH_2)_2 \xrightarrow{\Delta} NH_3 \uparrow + HCNO \quad (1)$$

The larger specific surface area ensures full infiltration of the active material and electrolyte, thereby shortening the transport path to accelerate the rapid transfer of Na^+/e^- [45]. The TiO_2 content of the composites was determined by TGA. As shown in Fig. S1, the weight losses of the composites are ~ 28.9% and 26.4% in air, which implies a TiO_2 content of 71.1 wt% in the TiO_2/N–C NFs and 73.6 wt% in the TiO_2–C NFs.

Figure 2a, b shows SEM images of the TiO_2–C NFs and TiO_2/N–C NFs, respectively. There is no obvious difference in the structural features of the TiO_2–C NFs and TiO_2/N–C NFs. Both samples show rough NFs with diameters from 100 to 130 nm. The structures of the TiO_2–C NFs and TiO_2/N–C NFs were further analyzed by TEM (Fig. 2c, d). The results show that TiO_2 particles are appropriately buried in the carbon matrix to develop a stable NF structure. Further, it can be seen, as intuitively expected, that the

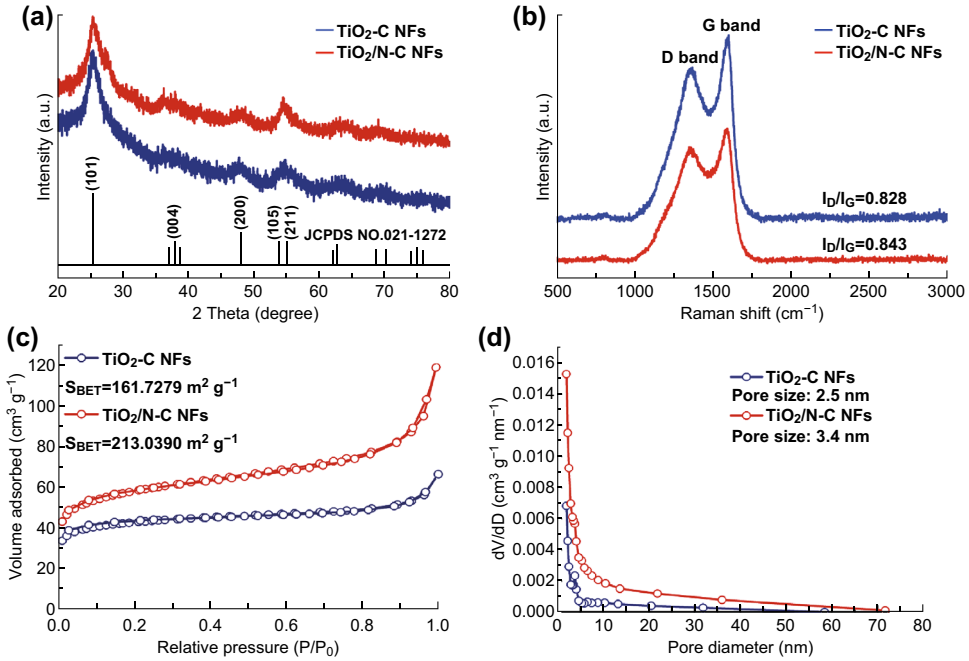

Fig. 1 **a** XRD patterns and **b** Raman spectra of TiO_2/N–C NFs and TiO_2–C NFs. **c** N_2 adsorption–desorption isotherms and **d** the corresponding pore size distributions of TiO_2/N–C NFs and TiO_2–C NFs

surface of the TiO_2/N–C NFs is rougher than that of the TiO_2–C NFs, so it can provide a larger specific surface area to help release more of the pseudocapacitor from the electrode materials [16]. The TEM mapping images of the TiO_2/N–C NFs in Fig. 2e reveal that C, N, Ti, and O are uniformly dispersed in the NFs. The high-resolution TEM (HRTEM) images in Fig. 2f clearly show lattice fringes of 0.35 and 0.24 nm in the nanoparticles, which correspond to the (101) and (103) planes of anatase-phase TiO_2, respectively.

The electrochemical performance was assessed by galvanostatic discharge–charge measurement in sodium half-cells. Figure 3a reveals the cycling properties of the TiO_2/N–C NF and TiO_2–C NF electrodes at 1 A g^{-1}. It is observed that the reversible discharge capacity of the TiO_2–C NF electrode can be maintained only at 94.9 mAh g^{-1} after 1000 cycles, and the corresponding capacity retention rate is 64.3% (relative to the discharge capacity of the second cycle). Under the same condition, the TiO_2/N–C NF electrode displays a much higher discharge capacity of 179.2 mAh g^{-1}, with a satisfactory capacity retention of 94.7%. The corresponding voltage curves of TiO_2/N–C NFs in different cycles are exhibited in Fig. 3b. The large capacity loss in the first cycle is associated mainly with the interface reaction between the active materials and electrolyte, which leads to the generation of a solid electrolyte interface (SEI) film [45, 46]. Further, as the number of cycles increases, the charge and discharge platform of the TiO_2/N–C NFs shows no significant change with respect to that of the TiO_2–C NFs (Fig. S2a), indicating excellent cycling stability.

Figure 3c shows the rate performance of the two samples. The TiO_2/N–C NF electrode could release reversible capacities of 265.8, 236.8, 202.4, 187.2, 175.6, 153.7, 136.4, and 132.1 mAh g^{-1} at current densities of 0.05, 0.1, 0.2, 0.5, 1, 2, 3, and 4 A g^{-1}, respectively. Even at 5 A g^{-1}, a reversible capacity of 124.5 mAh g^{-1} could be achieved. The discharge capacity could be maintained at 236.2 mAh g^{-1} when the current density recovered to 0.05 A g^{-1}, which represents an excellent rate capability. In contrast to that of the TiO_2/N–C NFs, the capacity of the TiO_2–C NFs decreased significantly as the current density increased and dropped to 43.1 mAh g^{-1} at 5 A g^{-1}. The outstanding rate properties may be due mainly to the improved conductivity resulting from the incorporation of N atoms. Figure 3d shows the corresponding discharge–charge curves. The discharge capacity of the TiO_2/N–C NFs gradually decreases with an increase in current density. Nonetheless, the TiO_2/N–C NF anode reveals less polarization than the TiO_2–C NF anode (Fig. S2b), which further demonstrates the excellent rate capability. An ultra-long-term high-rate cycling performance test was performed to further verify the electrochemical performance of the TiO_2/N–C NF anode. As shown in Fig. 3e, the specific capacity of the TiO_2/N–C NF anode remains at 118.1 mAh g^{-1} after 2000 cycles at 5 A g^{-1} and exhibits almost no capacity decay. In order to explore the effect of adding urea to the precursor solution on the TiO_2/N–C NF

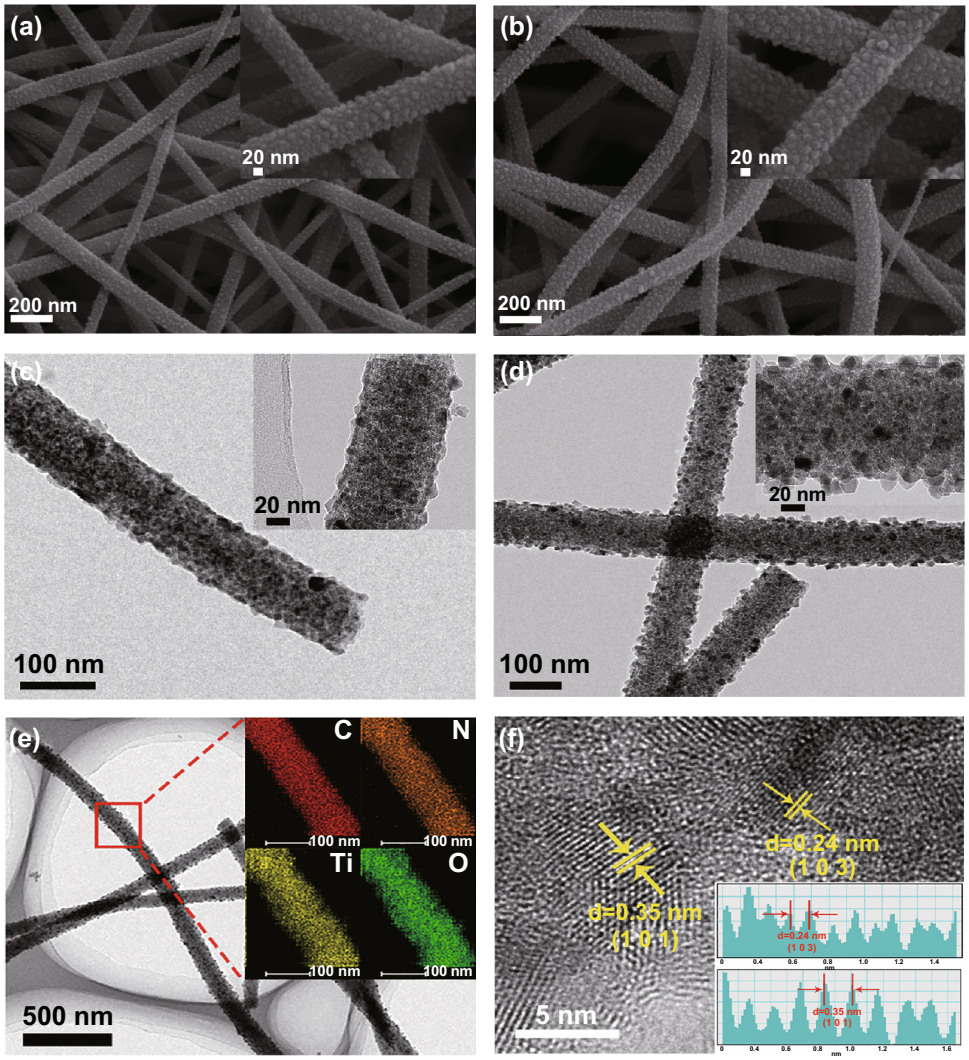

Fig. 2 SEM images of **a** TiO_2–C NFs and **b** TiO_2/N–C NFs. TEM images of **c** TiO_2–C NFs and **d** TiO_2/N–C NFs. **e** TEM elemental mapping images of C, N, Ti, and O in TiO_2/N–C NFs. **f** HRTEM image of TiO_2/N–C NFs with lattice spacing (the inset shows statistical tables of the interplanar crystal spacing)

anode, the electrochemical properties of samples with different amounts of urea (0.05, 0.1, and 0.2 g) are shown in Fig. S3. The composite with 0.1 g of added urea obviously exhibits the best cycle stability and rate performance.

In order to determine the mechanism of the outstanding cycling stability of the TiO_2/N–C NF electrode, a Na half-cell tested at a current density of 1 A g^{-1} for 1000 cycles was disassembled, and the morphology and microstructure of the TiO_2/N–C NF electrode after cycling were observed by TEM, as shown in Fig. S4a, b. The morphology of the TiO_2/N–C NFs remained essentially integrated. Further, as shown in the energy-dispersive X-ray spectroscopy (EDS) elemental mapping images in Fig. S4b, C, N, Ti, and O were still uniformly distributed in the NFs after a long cycling duration, indicating the mechanical stability of the fibers. Furthermore, the presence of Na in the EDS element mapping images also illustrates the process of sodium insertion/extraction during the cycle. An HRTEM image of the TiO_2/N–C NFs after 1000 cycles further reveals that the crystal structure of the TiO_2/N–C NFs remained integrated. From the above discussion, the preservation of the morphology and crystal structure of the TiO_2/N–C NF electrode after cycling further explains the excellent electrochemical properties.

Moreover, the rate capability of the TiO_2/N–C NFs is comparable with the previously reported results for many other TiO_2-based materials [47–53], which are presented in Fig. 4. It is clear that the TiO_2/N–C NFs in this work reveal a higher discharge capacity than most of the previously reported TiO_2-based materials at the same current density. Although a nitrogen-doped TiO_2 nanosphere anode shows higher discharge capacity at large current density, its cycle

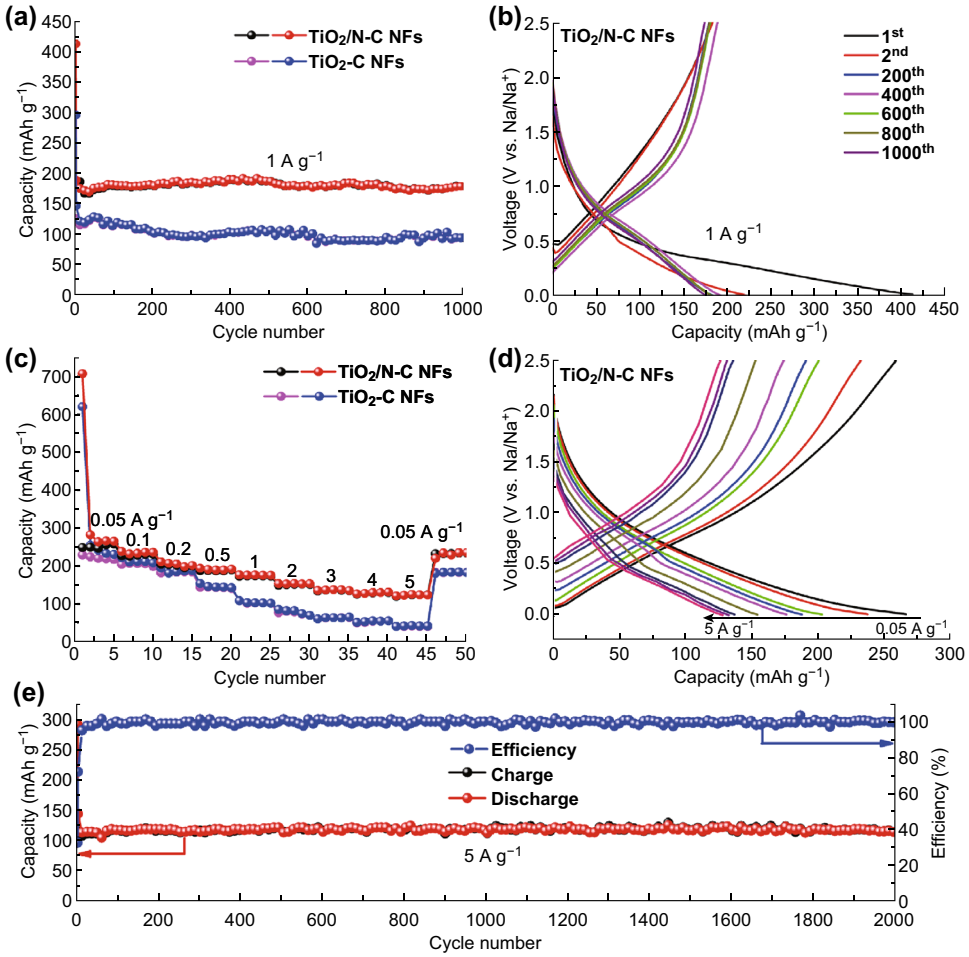

Fig. 3 **a** Cycling performance of the TiO_2/N–C NF and TiO_2–C NF electrodes under a current density of 1 A g^{-1}. **b** Continuous discharge and charge curves of TiO_2/N–C NF electrode under a current density of 1 A g^{-1}. **c** Rate capability of TiO_2/N–C NFs and TiO_2/C NFs. **d** Charge–discharge curves of TiO_2/N–C NFs at 0.05–5 A g^{-1} in the range of 0.01–2.5 V. **e** Long-term cycle performance of TiO_2/N–C NFs under a high current density of 5 A g^{-1}

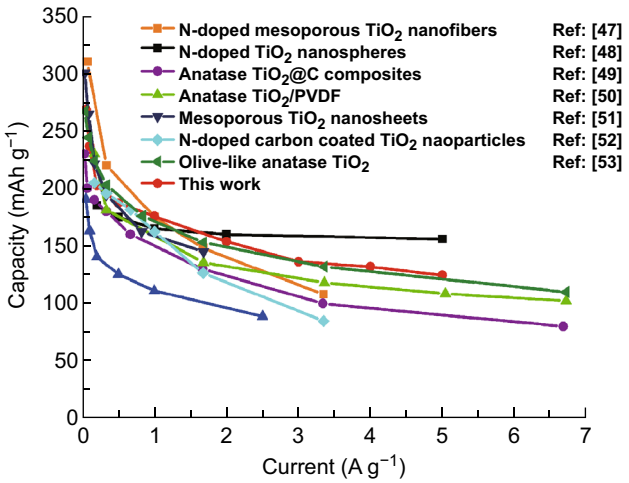

Fig. 4 Comparison of rate capability of TiO_2/N–C NFs with that of previously reported TiO_2-based composites with various morphologies

performance is inferior to that reported in this work [48]. The details are summarized in Table S1.

XPS was used to investigate the surface composition and chemical states of the samples. The survey XPS spectrum (Fig. 5a) shows the presence of C, N, Ti, and O in the two samples, and the N peak of the TiO_2/N–C NFs is significantly stronger than that of the TiO_2–C NFs, confirming the successful introduction of N atoms by nitrogen doping. To further understand the detailed information on each element, high-resolution C 1*s*, N 1*s*, and Ti 2*p* spectra of the TiO_2/N–C NFs are shown in Fig. 5b–d. In the C 1*s* region (Fig. 5b), both the TiO_2/N–C NF and TiO_2–C NF samples have three peaks at 284.84, 286.57, and 289.13 eV, which could correspond to C–C, C–O, and O–C=O, respectively [54, 55]. The main source of the C–O and O–C=O peaks is incomplete carbonization of PVP [56, 57]. Note that there is an additional peak at 286.04 eV corresponding to C=N for the TiO_2/N–C NFs, which further confirms the successful introduction of nitrogen [11].

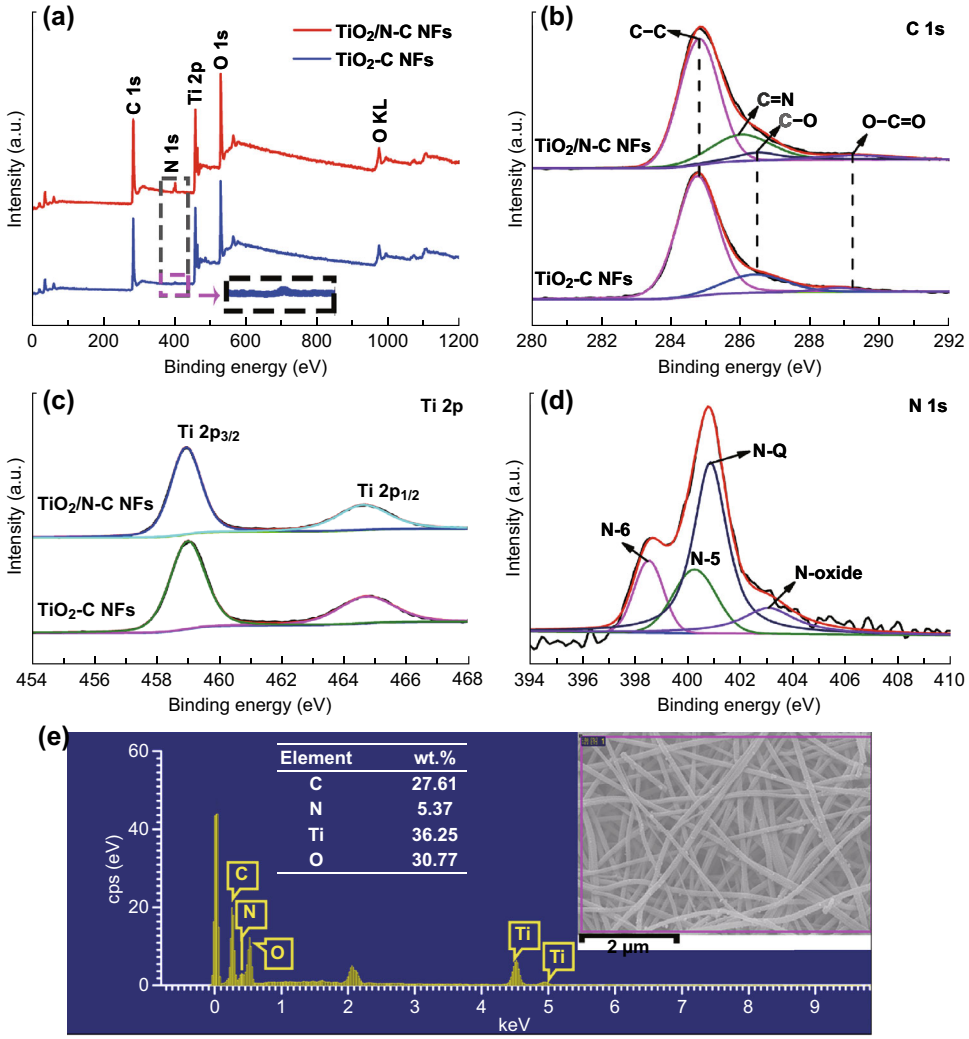

Fig. 5 **a** XPS wide scan spectra of TiO_2–C NFs and TiO_2/N–C NFs. High-resolution **b** C 1*s* and **c** Ti 2*p* XPS spectra of TiO_2–C NFs and TiO_2/N–C NFs. **d** High-resolution N 1*s* spectra of TiO_2/N–C NFs. **e** EDS spectrum of TiO_2/N–C NFs

In addition, the state of nitrogen from carbonization of PVP is significantly different from that in the TiO_2/N–C NFs (Fig. S5). It is obvious that the N-oxide peak does not appear in the spectrum of the TiO_2–C NFs, possibly because the N content of the composite is too small. Thus, the introduction of urea does change the content and state of nitrogen significantly. As shown in Fig. 5c, peaks situated at approximately 458.97 and 464.67 eV could be observed for the two samples, indicating the presence of Ti^{4+} in TiO_2 [21, 58]. In the N 1*s* spectrum of the TiO_2/N–C NFs (Fig. 5d), four forms of nitrogen in carbon can be observed: pyridinic N (N-6) at 398.47 eV, pyrrolic/pyridone N (N-5) at 400.05 eV, quaternary N (N-Q) at 401.01 eV, and pyridine-N-oxide at 403.19 eV [59, 60]. These different types of nitrogen are shown schematically in Fig. 6e. Quaternary N located inside the graphene layer is also called graphitic N and will improve the electric conductivity of the carbon layer because it can provide excess free electrons. Other N atoms including pyrrolic N, pyridinic N, and oxidized N atoms, located at the edge or in the defects of the carbon layer, can provide active sites for Na^+ insertion to enhance the Na^+ storage capacity [61, 62]. The elemental distribution in the TiO_2/N–C NFs was further investigated using the EDS spectrum (Fig. 5e), and the nitrogen content of the TiO_2/N–C NFs was found to be 5.37 wt%.

Figure 6a–c shows the nitrogen content of TiO_2/N–C NFs with different amounts of added urea. As shown in Fig. 6d, it is clear that the N-6 and N-Q contents continue to decline and the N-5 and N-oxide contents constantly increase with an increase in N content in the carbon layer. Along with the total N content, the specific percentages of diverse N species in various TiO_2/N–C NF materials are displayed in Table 1. Specifically, TiO_2/N–C NFs with 0.1 g of added urea have the highest N-Q content, which can ensure excellent conductivity in the electrode material.

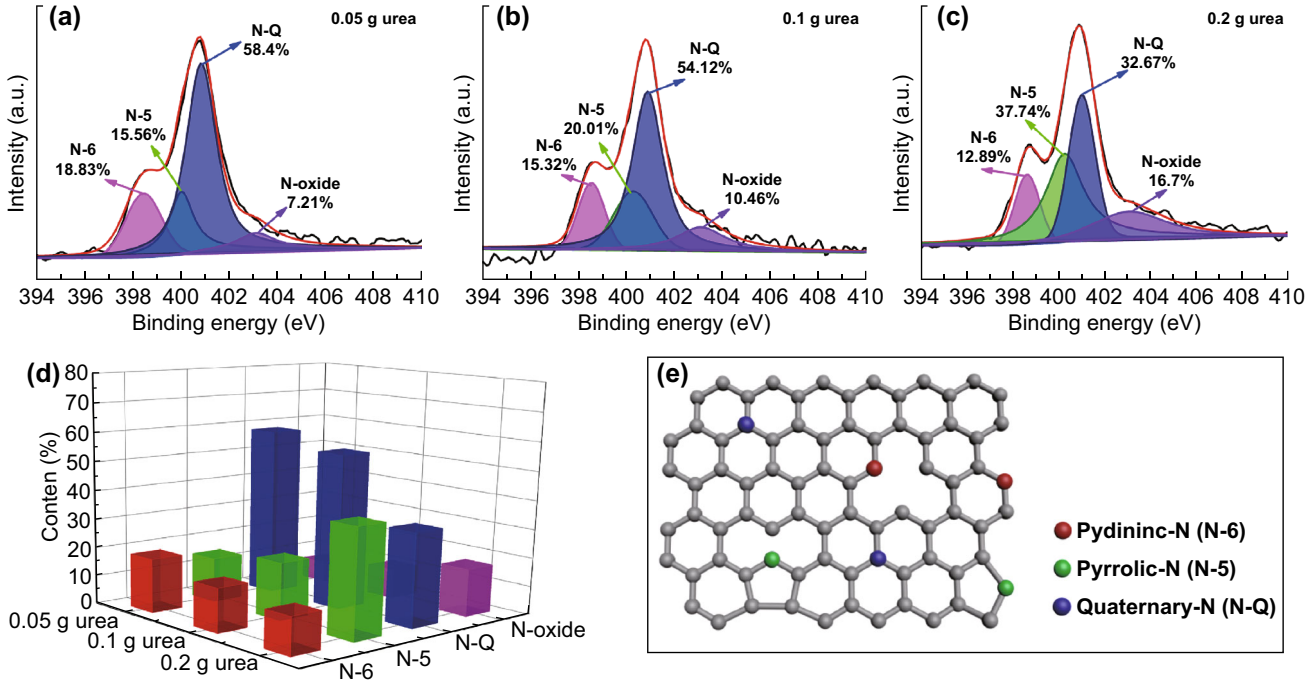

Fig. 6 N 1*s* fine spectra of TiO_2/N–C NFs with **a** 0.05 g, **b** 0.1 g, and **c** 0.2 g of added urea. **d** Histogram of ratio of different N species in various TiO_2/N–C NF samples. **e** Schematic of structural binding conditions of nitrogen

Table 1 Nitrogen content of samples to which different amounts of urea were added

Nitrogen content (wt%)					
Sample	Total (%)	N-6	N-5	N-Q	N-oxide
N–TiO_2/C NFs (0.05 g urea)	4.64	0.87	0.72	2.71	0.34
N–TiO_2/C NFs (0.1 g urea)	5.37	0.82	1.07	2.92	0.56
N–TiO_2/C NFs (0.2 g urea)	6.02	0.77	2.27	1.97	1.01

This may be the main reason that this sample shows the best electrochemical performance among the samples with different amounts of added urea, as shown in Fig. S3.

The CV curves of the TiO_2/N–C NF and TiO_2–C NF electrodes at 0.1 mV s^{-1} are shown in Fig. 7a, b, respectively. Both of the electrodes show a pair of wide anodic/cathodic peaks at a potential of 0.76/0.63 V, which corresponds to Na^+ extraction/insertion to/from the anatase TiO_2 [48]. Further, there is a large gap between the first cycle and the next few cycles, which can be attributed to the generation of an SEI by decomposition of the electrolyte in the initial cycle, resulting in a low coulombic efficiency in the initial charge–discharge process [45]. The shape and intensity of the curves are highly consistent after the second cycle, implying satisfactory stability of these materials.

CV curves at scan rates of 0.1–10 mV s^{-1} were obtained to investigate the kinetic behaviors of the TiO_2/N–C NFs (Fig. 7c). Obvious distortion from the basic shape can be found in the CV curves as the sweep rate increases. Several factors, such as ohmic resistance and/or diffusion constraints, are responsible for the distortion. Figure 7d shows the linear relationship between the logarithms of the sweep rates and the redox peak currents related to Na^+ insertion/extraction in the TiO_2/N–C NFs. The dominant charge storage mechanism is given by Eq. 2:

$$i = av^b \tag{2}$$

In this equation, the response current (i) and scan rate (v) are subject to a power-law relationship, and the value of b can be obtained from the slope (lg i vs. lg v). A b value of 0.5 indicates a diffusion-dominated process, and a b value of 1 suggests a capacitive-controlled process [63, 64]. The b values of both the cathodic (0.87) and anodic (0.83) peaks are larger than 0.7, indicating a pseudocapacitive process between the typical behaviors of batteries and capacitors [65]. Further, the contribution of these two mechanisms to the total charge storage can be determined by Eqs. 3 and 4:

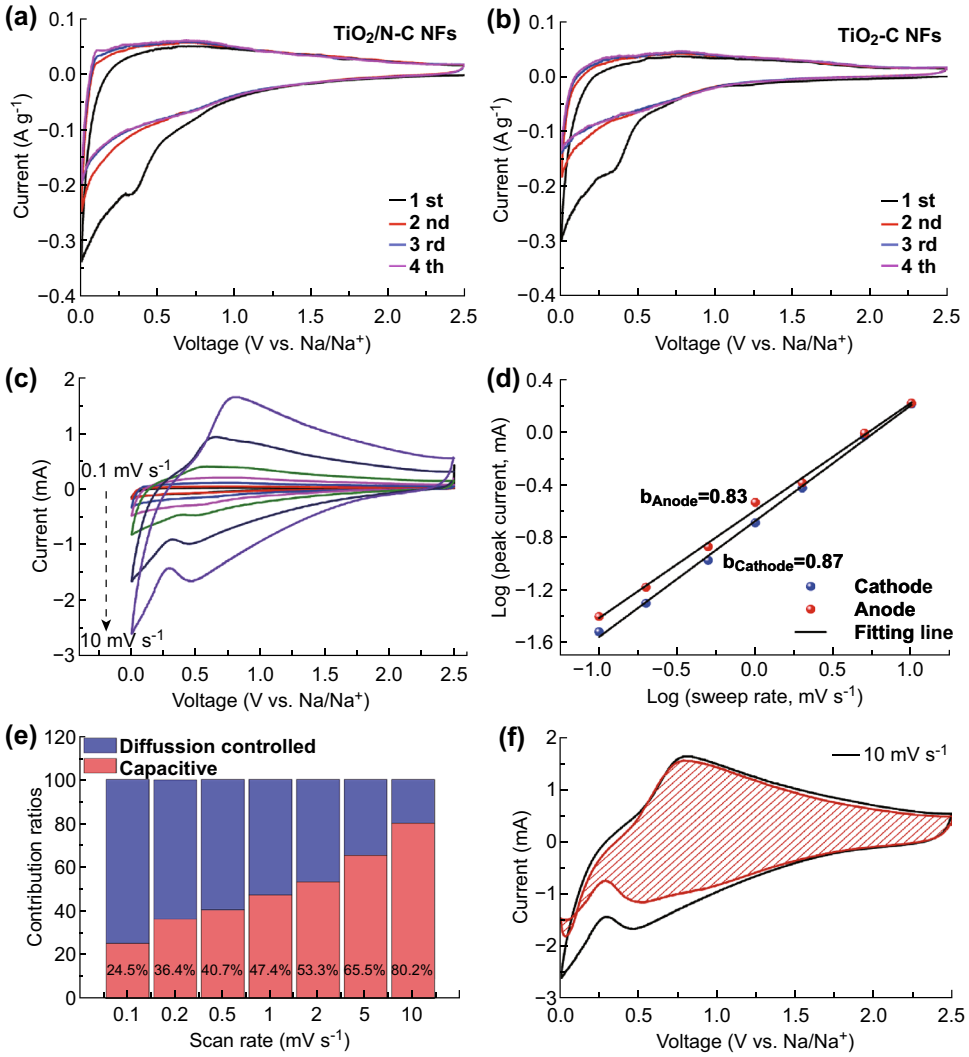

Fig. 7 CV curves of **a** the TiO_2/N–C NF electrode and **b** the TiO_2–C NF electrode at a scan rate of 0.1 mV s^{-1}. **c** CV plots of TiO_2/N–C NFs at various sweep rates from 0.1 to 10 mV s^{-1}. **d** Relationship between the peak currents and scan rates in logarithmic scale. **e** Diagram of capacitive contribution to the total capacity of TiO_2/N–C NFs at different scan rates. **f** CV curve of TiO_2/N–C NFs (black curve) and capacitive contribution measured at 10 mV s^{-1} (red-shaded region). (Color figure online)

$$i = k_1 v + k_2 v^{1/2} \tag{3}$$

$$\text{or } i/v^{1/2} = k_1 v^{1/2} + k_2 \tag{4}$$

where $k_1 v$ represents the contribution of the surface capacitive effects, and $k_2 v^{1/2}$ corresponds to the contribution of intercalation/deintercalation effects. The fraction of the current response from these contributions to the specific potentials can be quantified by determining k_1 and k_2.

As the pseudocapacitive energy storage occurs on the surface or near the surface of the electrode, the ion diffusion is a type of diffusion on the surface or in the liquid phase, which has a much faster velocity than that in the solid phase. The characteristics of rapid ion diffusion greatly increase the ability of electrode materials to charge and discharge rapidly at high current densities [63, 66–68]. As shown in Fig. 7e, the contribution of the pseudocapacitance to the overall capacity increases with an increase in scan rate. Specifically, the contribution of the capacitive effect to the total charge stored at 0.1 mV s^{-1} is 24.5% and increases to 80.2% at 10 mV s^{-1} (Fig. 7f). However, the TiO_2–C NFs show a low pseudocapacitance contribution of 16.2% at 0.1 mV s^{-1}, and the value is only 67.4% even at 10 mV s^{-1} (Fig. S3). The large contribution of the pseudocapacitive contribution to the overall capacity may be correlated with the large specific surface area and the participation of nitrogen, which cause the TiO_2/N–C NFs to exhibit excellent electrochemical performance as an anode in SIBs at ultra-high current density.

The dynamical properties of the TiO_2/N–C NF electrode were explored through EIS measurement. As shown in Fig. 8a, the EIS patterns consist mainly of three parts: a

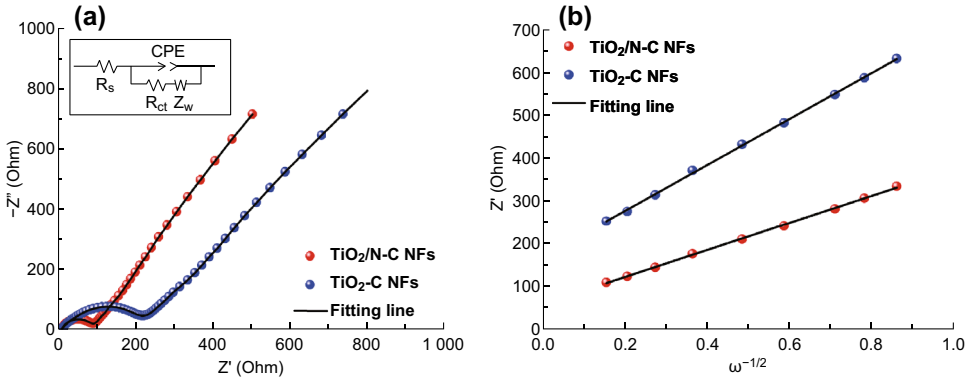

Fig. 8 **a** Nyquist plots of TiO_2/N–C NF and TiO_2–C NF electrodes measured after the first cycle at 0.05 A g^{-1}. (The inset shows the equivalent circuit model.) **b** Relationship between Z' and $\omega^{-1/2}$ at low frequency

small intercept in the high-frequency region (R_s), a semicircle in the high-frequency region (R_{ct}), and a sloping line in the low-frequency region (Z_w). R_s, R_{ct}, and Z_w represent the resistance of the electrolyte in contact with particles, the charge transfer resistance, and Na^+ ion diffusion in the anode active material, respectively [69, 70]. According to the fitted experimental data, the TiO_2/N–C NFs show a lower R_{ct} value (85.5 Ω) than the TiO_2–C NFs (210.3 Ω), indicating that the introduction of nitrogen can enhance the kinetics of the electrochemical reaction according to Eq. 5

$$i_0 = RT/nFR_{ct} \tag{5}$$

where i_0 represents the exchange current density, R is the gas constant, T is the temperature in Kelvin, F is the Faraday constant, and n is the number of electrons per molecule during the electronic transfer reaction. The value of i_0 can be used to measure the resistance of the electrode (the higher the value, the lower the electrical resistance) [71]. The diffusion coefficient of sodium ions (D_{Na+}) can be calculated using Eqs. 6 and 7:

$$D_{Na^+} = \frac{R^2T^2}{2A^2n^4F^4c^2\sigma_w^2} \tag{6}$$

$$Z' = R_s + R_{ct} + \sigma_w\omega^{-1/2} \tag{7}$$

where A is the surface area of the electrode, c is the concentration of sodium ions, and σ_w is the Warburg factor, which can be obtained by calculating the slope of the line Z'–$\omega^{-1/2}$, as shown in Fig. 8b. Table 2 shows that the D_{Na+} value of the TiO_2/N–C NFs (5.8×10^{-13} cm^2 s^{-1}) is approximately 2.9 times higher than that of the TiO_2–C NFs (2.0×10^{-13} cm^2 s^{-1}). The increased diffusion coefficient of sodium ions (D_{Na+}) may be attributed mainly to the incorporation of nitrogen atoms and brings about the better electrochemical performance of the TiO_2/N–C NF electrode.

Table 2 Comparison of EIS parameters of TiO_2/N–C NFs and TiO_2/C NFs

Samples	R_s (Ω)	R_{ct} (Ω)	I_0 (mA cm^{-2})	D_{Na+} (cm^2 s^{-1})
N–TiO_2/C NFs	7.33	85.5	0.30	5.8×10^{-13}
TiO_2/C NFs	6.97	210.3	0.12	2.0×10^{-13}

The Nyquist plots of the TiO_2/N–C NFs with different amounts of urea are used to explain the causes of these different electrochemical properties (Fig. S7). The simulated results are shown in Table S2. It can be seen that the R_s values of TiO_2/N–C NFs with different amounts of urea are similar. However, the R_{ct} value of TiO_2/N–C NFs with 0.1 g of added urea is 85.5 Ω, which is smaller than that of the TiO_2/N–C NFs with 0.05 g of added urea and much smaller than that of TiO_2/N–C NFs with 0.2 g of added urea. Hence, it can be deduced that TiO_2/N–C NFs with 0.1 g of added urea exhibit the smallest electrochemical resistance, indicating the best electron conductivity and electrochemical activity.

4 Conclusions

In summary, nitrogen-doped TiO_2–C composite NFs were fabricated by a facile and green electrospinning method. Inexpensive urea was used as a nitrogen source and pore-forming agent. The as-prepared TiO_2/N–C NFs exhibited a large specific surface area (213.04 m^2 g^{-1}) and a suitable nitrogen content (5.37 wt%). These characteristics not only contribute to increasing the contact area with the electrolyte and thus shortening the ion/electron diffusion distance, but also essentially enhance the electronic conductivity. As anodes in SIBs, the TiO_2/N–C NFs exhibit a high reversible capacity (265.8 mAh g^{-1} at 0.05 A g^{-1}), an outstanding rate performance (202.4 and 153.7 mAh g^{-1} at 0.2 and 2 A g^{-1}, respectively), and an ultra-long cycling durability (118.1 mAh g^{-1} at 5 A g^{-1}

after 2000 cycles). This work will open the way to the use of TiO_2/N–C NFs as one of the most promising anode materials for low-cost SIBs.

Acknowledgements This work was supported financially by the National Natural Science Foundation of China (Grant No. 51672234), Hunan 2011 Collaborative Innovation Center of Chemical Engineering and Technology with Environmental Benignity and Effective Resource Utilization, Program for Innovative Research Cultivation Team in University of Ministry of Education of China (1337304), and the 111 Project (B12015).

References

1. M. Mao, F. Yan, C. Cui, J. Ma, M. Zhang, T. Wang, C. Wang, Pipe-wire TiO_2–Sn@Carbon nanofibers paper anodes for lithium and sodium ion batteries. Nano Lett. **17**(6), 3830–3836 (2017). https://doi.org/10.1021/acs.nanolett.7b01152
2. J. Cabana, L. Monconduit, D. Larcher, M.R. Palacín, Beyond intercalation-based Li-ion batteries: the state of the art and challenges of electrode materials reacting through conversion reactions. Adv. Mater. **22**(35), 170 (2010). https://doi.org/10.1002/adma.201000717
3. M.V. Reddy, G.V. Subba Rao, B.V.R. Chowdari, Metal oxides and oxysalts as anode materials for Li ion batteries. Chem. Rev. **113**(7), 5364–5457 (2013). https://doi.org/10.1021/cr3001884
4. J. Liang, H. Hu, H. Park, C. Xiao, S. Ding, U. Paik, X.W. Lou, Construction of hybrid bowl-like structures by anchoring NiO nanosheets on flat carbon hollow particles with enhanced lithium storage properties. Energy Environ. Sci. **8**(6), 1707–1711 (2015). https://doi.org/10.1039/C5EE01125F
5. J. Xie, L. Liu, J. Xia, Y. Zhang, M. Li, Y. Ouyang, S. Nie, X. Wang, Template-free synthesis of Sb_2S_3 hollow microspheres as anode materials for lithium-ion and sodium-ion batteries. Nano-Micro Lett. **10**(1), 12 (2018). https://doi.org/10.1007/s40820-017-0165-1
6. M.B. Vazquez-Santos, P. Tartaj, E. Morales, J.M. Amarilla, TiO_2 nanostructures as anode materials for Li/Na-ion batteries. Chem. Rec. **18**(7–8), 1178–1191 (2018). https://doi.org/10.1002/tcr.201700103
7. H. He, Q. Gan, H. Wang, G.L. Xu, X. Zhang et al., Structure-dependent performance of TiO_2/C as anode material for Na-ion batteries. Nano Energy **44**, 217 (2018). https://doi.org/10.1016/j.nanoen.2017.11.077
8. Z. Yan, L. Liu, H. Shu, X. Yang, H. Wang, J. Tan, Q. Zhou, Z. Huang, X. Wang, A tightly integrated sodium titanate–carbon composite as an anode material for rechargeable sodium ion batteries. J. Power Sources **274**, 8–14 (2015). https://doi.org/10.1016/j.jpowsour.2014.10.045
9. Z. Yan, L. Liu, J. Tan, Q. Zhou, Z. Huang, D. Xia, H. Shu, X. Yang, X. Wang, One-pot synthesis of bicrystalline titanium dioxide spheres with a core–shell structure as anode materials for lithium and sodium ion batteries. J. Power Sources **269**(269), 37–45 (2014). https://doi.org/10.1016/j.jpowsour.2014.06.150
10. Y. Liu, N. Zhang, L. Jiao, J. Chen, Tin nanodots encapsulated in porous nitrogen-doped carbon nanofibers as a free-standing anode for advanced sodium-ion batteries. Adv. Mater. **27**(42), 6702–6707 (2016). https://doi.org/10.1002/adma.201503015
11. S. Wang, L. Xia, L. Yu, L. Zhang, H. Wang, X.W. Lou, Free-standing nitrogen-soped carbon nanofiber films: integrated electrodes for sodium-ion batteries with ultralong cycle life and superior rate capability. Adv. Energy Mater. **6**(7), 1502217 (2016). https://doi.org/10.1002/aenm.201502217
12. Y. Kim, Y. Kim, A. Choi, S. Woo, D. Mok et al., Tin phosphide as a promising anode material for Na-ion batteries. Adv. Mater. **26**(24), 4139–4144 (2014). https://doi.org/10.1002/adma.201305638
13. J. Qian, Y. Chen, L. Wu, Y. Cao, X. Ai, H. Yang, High capacity Na-storage and superior cyclability of nanocomposite Sb/C anode for Na-ion batteries. Chem. Commun. **48**(56), 7070–7072 (2012). https://doi.org/10.1039/c2cc32730a
14. K. Zhang, M. Park, L. Zhou, G.-H. Lee, J. Shin, Z. Hu, S.-L. Chou, J. Chen, Y.-M. Kang, Cobalt-doped FeS_2 nanospheres with complete solid solubility as a high-performance anode material for sodium-ion batteries. Angew. Chem. Int. Ed. **55**(41), 12822–12826 (2016). https://doi.org/10.1002/anie.201607469
15. N. Zhang, X. Han, Y. Liu, X. Hu, Q. Zhao, J. Chen, 3D porous γ-Fe_2O_3@C nanocomposite as high-performance anode material of Na-ion batteries. Adv. Energy Mater. **5**, 1401123 (2015). https://doi.org/10.1002/aenm.201401123
16. F. Xie, L. Zhang, D. Su, M. Jaroniec, S.Z. Qiao, $Na_2Ti_3O_7$@N-doped carbon hollow spheres for sodium-ion batteries with excellent rate performance. Adv. Mater. **29**(24), 1700989 (2017). https://doi.org/10.1002/adma.201700989
17. S.M. Oh, J.Y. Hwang, C.S. Yoon, J. Lu, K. Amine, I. Belharouak, Y.K. Sun, High electrochemical performances of microsphere C–TiO_2 anode for sodium-ion battery. ACS Appl. Mater. Interfaces **6**(14), 11295–11301 (2014). https://doi.org/10.1021/am501772a
18. Y.E. Zhu, L. Yang, J. Sheng, Y. Chen, H. Gu, J. Wei, Z. Zhou, Fast sodium storage in TiO_2@CNT@C nanorods for high-performance Na-ion capacitors. Adv. Energy Mater. **7**(22), 1701222 (2017). https://doi.org/10.1002/aenm.201701222
19. Y. Yang, X. Ji, M. Jing, H. Hou, Y. Zhu, L. Fang, X. Yang, Q. Chen, C.E. Banks, Carbon dots supported upon N-doped TiO_2 nanorods applied into sodium and lithium ion batteries. J. Mater. Chem. A **3**, 5648 (2015). https://doi.org/10.1039/C4TA05611F
20. Y. Yang, W. Shi, S. Liao, R. Zhang, S. Leng, Black defect-engineered TiO_2 nanocrystals fabricated through square-wave alternating voltage as high-performance anode materials for lithium-ion batteries. J. Alloys Compd. **746**, 619–625 (2018). https://doi.org/10.1016/j.jallcom.2018.02.309
21. Q. Zhang, H. He, X. Huang, J. Yan, Y. Tang, H. Wang, TiO_2@C nanosheets with highly exposed (0 0 1) facets as a high-capacity anode for Na-ion batteries. Chem. Eng. J. **332**, 57 (2018). https://doi.org/10.1016/j.cej.2017.09.044
22. Y. Liu, F. Zhao, J. Li, Y. Li, J.A. McLeod, L. Liu, Influence of crystal phase on TiO_2 nanowire anodes in sodium ion batteries. J. Mater. Chem. A **5**, 20005–20013 (2017). https://doi.org/10.1039/C7TA05852G
23. H.A. Cha, H.M. Jeong, J.K. Kang, Nitrogen-doped open pore channeled graphene facilitating electrochemical performance of TiO_2 nanoparticles as an anode material for sodium ion batteries. J. Mater. Chem. A **2**(15), 5182–5186 (2014). https://doi.org/10.1039/C4TA00041B
24. H. Xiong, M.D. Slater, M. Balasubramanian, C.S. Johnson, T. Rajh, Amorphous TiO_2 nanotube anode for rechargeable sodium ion batteries. J. Phys. Chem. Lett. **2**(20), 2560–2565 (2011). https://doi.org/10.1021/jz2012066
25. Y. Lai, W. Liu, J. Li, K. Zhang, F. Qin, M. Wang, J. Fang, High performance sodium storage of Fe-doped mesoporous anatase

TiO_2/amorphous carbon composite. J. Alloys Compd. **666**, 254–261 (2016). https://doi.org/10.1016/j.jallcom.2016.01.101
26. J. Ni, S. Fu, C. Wu, J. Maier, Y. Yu, L. Li, Self-supported nanotube arrays of sulfur-doped TiO_2 enabling ultrastable and robust sodium storage. Adv. Mater. **28**(11), 2259–2265 (2016). https://doi.org/10.1002/adma.201504412
27. H. Usui, S. Yoshioka, K. Wasada, M. Shimizu, H. Sakaguchi, Nb-doped rutile TiO_2: a potential anode material for Na-ion battery. ACS Appl. Mater. Interfaces **7**(12), 6567–6573 (2015). https://doi.org/10.1021/am508670z
28. Y. Yang, S. Liao, W. Shi, Y. Wu, R. Zhang, S. Leng, Nitrogen-doped TiO_2(B) nanorods as high-performance anode materials for rechargeable sodium-ion batteries. RSC Adv. **7**(18), 10885–10890 (2017). https://doi.org/10.1039/C7RA00469A
29. H.M. Jeong, J.W. Lee, W.H. Shin, Y.J. Choi, H.J. Shin, J.K. Kang, J.W. Choi, Nitrogen-doped graphene for high-performance ultracapacitors and the importance of nitrogen-doped sites at basal planes. Nano Lett. **11**(6), 2472–2477 (2011). https://doi.org/10.1021/nl2009058
30. P. Zhu, J. Song, D. Lv, D. Wang, C. Jaye, D.A. Fischer, T. Wu, Y. Chen, Mechanism of enhanced carbon cathode performance by nitrogen doping in lithium-sulfur battery: an X-ray absorption spectroscopic study. J. Phys. Chem. C **118**(15), 7765–7771 (2014). https://doi.org/10.1021/jp4123634
31. Z. Wang, Q. Long, L. Yuan, W. Zhang, X. Hu, Y. Huang, Functionalized N-doped interconnected carbon nanofibers as an anode material for sodium-ion storage with excellent performance. Carbon **55**(2), 328–334 (2013). https://doi.org/10.1016/j.carbon.2012.12.072
32. D. Li, H. Chen, G. Liu, M. Wei, L.X. Ding, S. Wang, H. Wang, Porous nitrogen doped carbon sphere as high performance anode of sodium-ion battery. Carbon **94**, 888–894 (2015). https://doi.org/10.1016/j.carbon.2015.07.067
33. Y. He, P. Xu, B. Zhang, Y. Du, B. Song, X. Han, H. Peng, Ultrasmall MnO nanoparticles supported on nitrogen-doped carbon nanotubes as efficient anode materials for sodium ion batteries. ACS Appl. Mater. Interfaces **9**(44), 38401 (2017). https://doi.org/10.1021/acsami.7b09559
34. T. Guo, H. Liao, P. Ge, Y. Zhang, Y. Tian, W. Hong, Z. Shi, Fe_2O_3 embedded in the nitrogen-doped carbon matrix with strong C–O–Fe oxygen-bridge bonds for enhanced sodium storages. Mater. Chem. Phys. **216**, 58 (2018). https://doi.org/10.1016/j.matchemphys.2018.05.054
35. Y. Wang, C. Wang, Y. Wang, H. Liu, Z. Huang, Superior sodium-ion storage performance of Co_3O_4@nitrogen-doped carbon: derived from a metal-organic framework. J. Mater. Chem. A **4**(15), 5428–5435 (2016). https://doi.org/10.1039/C6TA00236F
36. Y. Zhang, C. Wang, H. Hou, G. Zou, X. Ji, Nitrogen doped/carbon tuning yolk-like TiO_2 and its remarkable impact on sodium storage performances. Adv. Energy Mater. **7**, 1600173 (2017). https://doi.org/10.1002/aenm.201600173
37. J. Xia, L. Liu, S. Jamil, J. Xie, H. Yan et al., Free-standing SnS/C nanofiber anodes for ultralong cycle-life lithium-ion batteries and sodium-ion batteries. Energy Storage Mater. (in press) (2018). https://doi.org/10.1016/j.ensm.2018.08.005
38. T. Jin, Y. Liu, Y. Li, K. Cao, X. Wang, L. Jiao, Electrospun $NaVPO_4F$/C nanofibers as self-standing cathode material for ultralong cycle life Na-ion batteries. Adv. Energy Mater. **7**(15), 1700087 (2017). https://doi.org/10.1002/aenm.201700087
39. B. Wang, J.L. Cheng, Y.P. Wu, D. Wang, D.N. He, Porous NiO fibers prepared by electrospinning as high performance anode materials for lithium ion batteries. Electrochem. Commun. **23**(8), 5–8 (2012). https://doi.org/10.1016/j.elecom.2012.07.003
40. T. Jin, Q. Han, Y. Wang, L. Jiao, 1D nanomaterials: design, synthesis, and applications in sodium-ion batteries. Small **14**(2), 1703086 (2018). https://doi.org/10.1002/smll.201703086
41. Y. Zhong, M. Yang, X. Zhou, Y. Luo, J. Wei, Z. Zhou, Orderly packed anodes for high-power lithium-ion batteries with super-long cycle life: rational design of $MnCo_3$/large-area graphene composites. Adv. Mater. **27**(5), 806–812 (2015). https://doi.org/10.1002/adma.201404611
42. L. Sun, C. Tian, Y. Fu, Y. Yang, J. Yin, L. Wang, H. Fu, Nitrogen-doped porous graphitic carbon as an excellent electrode material for advanced supercapacitors. Chem. Eur. J. **20**(2), 564–574 (2014). https://doi.org/10.1002/chem.201303345
43. C.N. Schmidt, G. Cao, Properties of mesoporous carbon modified carbon felt for anode of all-vanadium redox flow battery. Sci. China Mater. **59**(12), 1037–1050 (2016). https://doi.org/10.1007/s40843-016-5114-8
44. J. Hou, C. Cao, F. Idrees, X. Ma, Hierarchical porous nitrogen-doped carbon nanosheets derived from silk for ultrahigh-capacity battery anodes and supercapacitors. ACS Nano **9**(3), 2556 (2015). https://doi.org/10.1021/nn506394r
45. S. Anwer, Y. Huang, J. Liu, J. Liu, M. Xu, Z. Wang, R. Chen, J. Zhang, F. Wu, Nature-inspired $Na_2Ti_3O_7$ nanosheets-formed three-dimensional microflowers architecture as a high-performance anode material for rechargeable sodium-ion batteries. ACS Appl. Mater. Interfaces **9**(13), 11669–11677 (2017). https://doi.org/10.1021/acsami.7b01519
46. D. Xu, C. Chen, J. Xie, B. Zhang, L. Miao, J. Cai, Y. Huang, L. Zhang, A hierarchical N/S-codoped carbon anode fabricated facilely from cellulose/polyaniline microspheres for high-performance sodium-ion batteries. Adv. Energy Mater. **6**(6), 1501929 (2016). https://doi.org/10.1002/aenm.201501929
47. Y. Wu, X. Liu, Z. Yang, L. Gu, Y. Yu, Nitrogen-doped ordered mesoporous anatase TiO_2 nanofibers as anode materials for high performance sodium-ion Batteries. Small **12**(26), 3474 (2016). https://doi.org/10.1002/smll.201670126
48. S. Liu, Z. Cai, J. Zhou, A. Pan, S. Liang, Nitrogen-doped TiO_2 nanospheres for advanced sodium-ion battery and sodium-ion capacitor applications. J. Mater. Chem. A **4**(47), 18278 (2016). https://doi.org/10.1039/C6TA08472A
49. X. Shi, Z. Zhang, K. Du, Y. Lai, J. Fang, J. Li, Anatase TiO_2@C composites with porous structure as an advanced anode material for Na ion batteries. J. Power Sources **330**, 1–6 (2016). https://doi.org/10.1016/j.jpowsour.2016.08.132
50. L. Ling, Y. Bai, Z. Wang, Q. Ni, G. Chen, Z. Zhou, C. Wu, Remarkable effect of sodium alginate aqueous binder on anatase TiO_2 as high-performance anode in sodium ion batteries. ACS Appl. Mater. Interfaces **10**(6), 5560 (2018). https://doi.org/10.1021/acsami.7b17659
51. R. Zhang, Y. Wang, H. Zhou, J. Lang, J. Xu, Mesoporous TiO_2 nanosheets anchored on graphene for ultra-long life Na-ion batteries. Nanotechnology **29**(22), 225401 (2018). https://doi.org/10.1088/1361-6528/aab562
52. J. Wang, G. Liu, K. Fan, D. Zhao, B. Liu, J. Jiang, D. Qian, C. Yang, J. Li, N-doped carbon coated anatase TiO_2 nanoparticles as superior Na-ion battery anodes. J. Colloid Interface Sci. **517**, 134–143 (2018). https://doi.org/10.1016/j.jcis.2018.02.001
53. J. Chen, Y. Zhang, G. Zou, Z. Huang, S. Li, H. Liao, J. Wang, H. Hou, X. Ji, Size-tunable olive-like anatase TiO_2 coated with carbon as superior anode for sodium-ion batteries. Small **12**(40), 5554–5563 (2016). https://doi.org/10.1002/smll.201601938
54. L. Shao, S. Quan, Y. Liu, Z. Guo, Z. Wang, A novel "gel–sol" strategy to synthesize TiO_2 nanorod combining reduced graphene oxide composites. Mater. Lett. **107**, 307–310 (2013). https://doi.org/10.1016/j.matlet.2013.06.050
55. Y.L. Huang, S.M. Yuen, C.C.M. Ma, C.Y. Chuang, K.C. Yu et al., Morphological, electrical, electromagnetic interference (EMI) shielding, and tribological properties of functionalized multi-walled carbon nanotube/poly methyl methacrylate

(PMMA) composites. Compos. Sci. Technol. **69**(11), 1991–1996 (2009). https://doi.org/10.1016/j.compscitech.2009.05.006
56. H. Wang, Q. Wu, D. Cao, X. Lu, J. Wang, M.K.H. Leung, S. Cheng, L. Lu, C. Niu, Synthesis of SnSb-embedded carbon–silica fibers via electrospinning: effect of TEOS on structural evolutions and electrochemical properties. Mater. Today Energy **1–2**, 24–32 (2016). https://doi.org/10.1016/j.mtener.2016.11.003
57. X. Lu, H. Wang, Z. Wang, Y. Jiang, D. Cao, G. Yang, Room-temperature synthesis of colloidal SnO_2 quantum dot solution and ex situ deposition on carbon nanotubes as anode materials for lithium ion batteries. J. Alloys Compd. **680**, 109–115 (2016). https://doi.org/10.1016/j.jallcom.2016.04.128
58. Y. Xu, E. Memarzadeh Lotfabad, H. Wang, B. Farbod, Z. Xu, A. Kohandehghan, D. Mitlin, Nanocrystalline anatase TiO_2: a new anode material for rechargeable sodium ion batteries. Chem. Commun. **49**(79), 8973–8975 (2013). https://doi.org/10.1039/c3cc45254a
59. H. Liu, M. Jia, N. Sun, B. Cao, R. Chen, Q. Zhu, F. Wu, N. Qiao, B. Xu, Nitrogen-rich mesoporous carbon as anode material for high-performance sodium-ion batteries. ACS Appl. Mater. Interfaces **7**(49), 27124 (2015). https://doi.org/10.1021/acsami.5b06898
60. C. Su, C. Pei, B. Wu, J. Qian, Y. Tan, Highly doped carbon nanobelts with ultrahigh nitrogen content as high-performance supercapacitor materials. Small **13**(29), 1700834 (2017). https://doi.org/10.1002/smll.201700834
61. F. Yang, Z. Zhang, K. Du, X. Zhao, W. Chen, Y. Lai, J. Li, Dopamine derived nitrogen-doped carbon sheets as anode materials for high-performance sodium ion batteries. Carbon **91**, 88–95 (2015). https://doi.org/10.1016/j.carbon.2015.04.049
62. J. Zhu, C. Chen, Y. Lu, Y. Ge, H. Jiang, K. Fu, X. Zhang, Nitrogen-doped carbon nanofibers derived from polyacrylonitrile for use as anode material in sodium-ion batteries. Carbon **94**, 189–195 (2015). https://doi.org/10.1016/j.carbon.2015.06.076
63. J. Wang, J. Polleux, J. Lim, B. Dunn, Pseudocapacitive contributions to electrochemical energy storage in TiO_2 (anatase) nanoparticles. J. Phys. Chem. C **111**(40), 14925–14931 (2007). https://doi.org/10.1021/jp074464w
64. F. Wen, H. Shu, Y. Zhang, J. Wan, W. Huang, X. Yang, R. Yu, L. Liu, X. Wang, Mesoporous $LiMnPO_4$/C nanoparticles as high performance cathode material for lithium ion batteries. Electrochim. Acta **214**, 85–93 (2016). https://doi.org/10.1016/j.electacta.2016.08.042
65. J. Ni, S. Fu, C. Wu, Y. Zhao, J. Maier, Y. Yu, L. Li, Superior sodium storage in $Na_2Ti_3O_7$ nanotube arrays through surface engineering. Adv. Energy Mater. **6**(11), 1502568 (2016). https://doi.org/10.1002/aenm.201502568
66. T. Brezesinski, J. Wang, S.H. Tolbert, B. Dunn, Ordered mesoporous α-MoO_3 with iso-oriented nanocrystalline walls for thin-film pseudocapacitors. Nat. Mater. **9**(2), 146–151 (2010). https://doi.org/10.1038/nmat2612
67. V. Augustyn, J. Come, M.A. Lowe, J.W. Kim, P.L. Taberna, S.H. Tolbert, H.D. Abruña, P. Simon, B. Dunn, High-rate electrochemical energy storage through Li^+ intercalation pseudocapacitance. Nat. Mater. **12**(6), 518 (2013). https://doi.org/10.1038/nmat3601
68. D. Kaufman, K.L. Hudson, R. Mcclamrock, Where do batteries end and supercapacitors begin? Science **343**(6176), 1210–1211 (2014). https://doi.org/10.1126/science.1249625
69. L. Yi, L. Liu, G. Guo, X. Chen, Y. Zhang, S. Yu, X. Wang, Expanded graphite@SnO_2@ polyaniline composite with enhanced performance as anode materials for lithium ion batteries. Electrochim. Acta **240**, 63 (2017). https://doi.org/10.1016/j.electacta.2017.04.012
70. L.-L. Zhang, S. Duan, X.-L. Yang, G. Peng, G. Liang, Y.-H. Huang, Y. Jiang, S.-B. Ni, M. Li, Reduced graphene oxide modified Li_2FeSiO_4/C composite with enhanced electrochemical performance as cathode material for lithium ion batteries. ACS Appl. Mater. Interfaces **5**(23), 12304–12309 (2013). https://doi.org/10.1021/am402434n
71. J. Lin, D. Ma, Y. Li, P. Zhang, H. Mi, L. Deng, L. Sun, X. Ren, In situ nitrogen doping of TiO_2 by plasma enhanced atomic layer deposition for enhanced sodium storage performance. Dalton Trans. **46**(38), 13101 (2017). https://doi.org/10.1039/C7DT03303F